5

High Spectral Resolution Lidar

Edwin E. Eloranta

Space Science and Engineering Center, University of Wisconsin–Madison,
1225 West Dayton Street, Madison, Wisconsin 53706, U.S.A
(eloranta@lidar.ssec.wisc.edu)

5.1 Introduction

Standard lidar systems provide profiles of the attenuated backscatter signal. These can be assembled into images with spatial and temporal resolution adequate for practically all problems of atmospheric research. However, the attenuated backscatter signal is a quantity that is composed of different atmospheric properties. Extremely valuable for an assessment of the state of the atmosphere, they are hard to extract from the measured profiles of the attenuated backscatter signal.

We start from the familiar lidar equation

$$P(r) = P_0 \eta \left(\frac{A}{r^2}\right) O(r) \left(\frac{ct}{2}\right) \beta(r) \exp\left[-2 \int_0^r \alpha(r')\mathrm{d}r'\right] \qquad (5.1)$$

in which $P(r)$ is the power received from range r, P_0 is the average transmitted power during the laser pulse, η is the receiver efficiency, A is the receiver area, r is the range to the scattering volume, $O(r)$ is the laser-beam receiver-field-of-view overlap function, c is the speed of light, t is the laser pulse duration, and β and α are the atmospheric backscatter coefficient and atmospheric extinction coefficient at range r (see Chapter 1). The integrated extinction coefficient

$$\tau(0, r) = \int_0^r \alpha(r)\mathrm{d}r \qquad (5.1a)$$

or, more generally,

$$\tau(r_1, r_2) = \int_{r_1}^{r_2} \alpha(r)\mathrm{d}r \tag{5.2}$$

is known as the optical depth or optical thickness of the atmosphere from the ground to height r or of a layer between r_1 and r_2, respectively.

Equation (5.1) relates profiles of one measured quantity with the profiles of the unknown atmospheric backscatter coefficient β and the unknown atmospheric extinction coefficient α. If we consider that each of these is the sum of a molecular and an aerosol component and that extinction, or the removal of light from a straight path through the atmosphere, is caused by both the part that is scattered and the part that is absorbed, or

$$\beta = \beta_{\mathrm{mol}} + \beta_{\mathrm{aer}} \quad \text{and} \tag{5.3}$$

$$\alpha = \alpha_{\mathrm{mol,sca}} + \alpha_{\mathrm{mol,abs}} + \alpha_{\mathrm{aer,sca}} + \alpha_{\mathrm{aer,abs}}, \tag{5.4}$$

then we have to solve Eq. (5.1) at each height for six unknowns, a task that is clearly impossible to carry out. Our knowledge of the atmosphere allows us to reduce the six primary unknowns to two by a procedure that, although well known, shall be briefly recalled here.

The magnitude of β_{mol} is obtained from Rayleigh scattering theory [1, 2]. β_{mol} obeys, for all practical purposes, a proportionality with atmospheric density. So if ground-level atmospheric temperature and pressure and the shape of one of the profiles (usually the temperature profile, from a radiosonde ascent or, better, a lidar) are known, then the profile of β_{mol} is also known. The proportionality factor is

$$\frac{\beta_{\mathrm{mol}}(r)}{\beta_{\mathrm{mol}}^{\mathrm{STP}}} = 1.47 \times 10^{-6} \times \left(\frac{550\,\mathrm{nm}}{\lambda}\right)^4 \mathrm{m}^{-1}\mathrm{sr}^{-1}, \tag{5.5}$$

with standard temperature and pressure (STP) defined as 0°C and 1013.25 hPa, conditions at which the atmosphere contains 2.69×10^{25} molecules per m^3 [3]. β_{aer} is also known as the absolute (nonnormalized) aerosol scattering phase function at scattering angle 180° or π, $\wp(\pi)$.

$\alpha_{\mathrm{mol,sca}}$ is strictly proportional to $\beta_{\mathrm{mol}}(r)$ and is given by

$$\alpha_{\mathrm{mol,sca}} = \beta_{\mathrm{mol}}(r) \times (8/3)\pi\,\mathrm{sr}. \tag{5.6}$$

$\alpha_{\mathrm{mol,abs}}$ is simply assumed to be zero. Clearly, this is not justified when, e.g., sizable concentrations of ozone are present and lidar wavelengths

are used at which ozone is known to absorb. Special techniques must then be used, e.g., correction algorithms based on the known concentration profiles measured with a lidar (see Chapter 7). β_{aer}, $\alpha_{\mathrm{aer,sca}}$, and $\alpha_{\mathrm{aer,abs}}$ are related with one another in a way determined by particle size, shape, and the real and imaginary part of the refractive index—provided the particles are homogeneous, which is not always the case. Clearly this relationship requires too much information and is too complicated to be useful for practical purposes. Therefore, $\alpha_{\mathrm{aer,sca}}$ and $\alpha_{\mathrm{aer,abs}}$ are considered together as one unknown $\alpha_{\mathrm{aer}} = \alpha_{\mathrm{aer,sca}} + \alpha_{\mathrm{aer,abs}}$, and β_{aer} as the other. This still leaves us with two unknown profiles to be determined from one profile of measured data.

Essentially two methods have been in use to solve the problem. One, known as the Klett method, is the assumption of a functional dependency of α_{aer} and β_{aer}, which then reduces the number of unknowns to one. This method is described and discussed in detail in Chapter 4; it suffers from the great variability of aerosols, which leads to deviations from the proportionality of α_{aer} and β_{aer} vital for the Klett method to work. Another is the measurement of two lidar profiles in one of which $\beta_{\mathrm{aer}} = 0$. This is the case in Raman lidar. Only molecules, not aerosols, contribute to the inelastic, i.e., frequency-shifted, Raman backscatter profile produced by molecular nitrogen and oxygen. From the fact that the elastic lidar return signal is affected by both α_{aer} and β_{aer}, but the Raman lidar return by α_{aer} alone, the two profiles can be solved for the two unknowns (Chapter 4). However, Raman scattering is weak; less than one photon will be scattered into one of the vibrational Raman lines for each thousand photons that are elastically scattered by a molecule. Furthermore, the spectrum of the scattered photons is broad, reflecting the large number of allowed rotational transitions of the scattering molecule. Raman lidars require powerful lasers and large telescopes in order to provide sufficient signal strength. Daytime operation is difficult because the small Raman signal must compete with scattered sunlight in the optical bandwidth required to collect the rotational lines of the Raman signal.

5.2 The Principle of High Spectral Resolution Lidar

Another idea based on the use of two measured profiles instead of just one is high spectral resolution lidar, or HSRL. This method utilizes the Doppler frequency shifts produced when photons are scattered

from molecules in random thermal motion. The Maxwellian distribution of molecular velocities has a width of ~300 m/s that produces Doppler shifts of ~1 GHz. In contrast, aerosols, cloud particles, and other particulate matter move with velocities determined by the wind (~10 m/s) and turbulence (~1 m/s) producing Doppler shifts of ~30 MHz and ~3 MHz, respectively. As a result, the frequency distribution of light backscattered from the atmosphere consists of a narrow spike near the frequency of the laser transmitter caused by particulate scattering riding on a much broader distribution produced by molecular scattering (see Fig. 5.1).

As in Raman lidar, there are two lidar equations instead of just one, but the structure of the equations is a lot more similar as only one wavelength is involved. Dropping the wavelength dependence, we have for

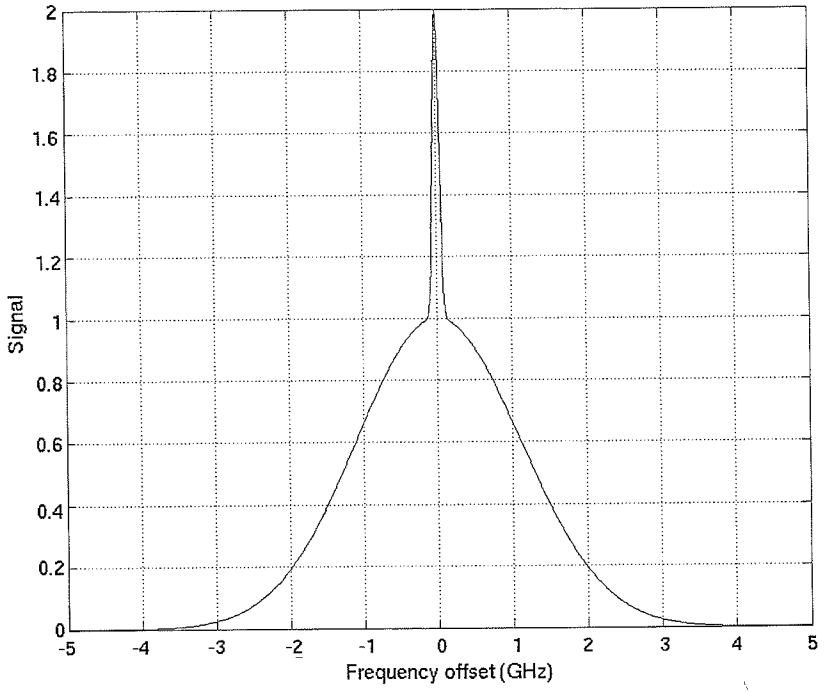

Fig. 5.1. Spectral profile of backscattering from a mixture of molecules and aerosols for a temperature of 300 K. The spectral width of the narrow aerosol return is normally determined by the line width of the transmitting laser.

the molecule and the aerosol signal

$$P_{\mathrm{mol}}(r) = K_{\mathrm{mol}} r^{-2} O(r) \beta_{\mathrm{mol}}(r) \exp\left(-2 \int_0^r \alpha(r')\mathrm{d}r'\right) \text{ and} \quad (5.7)$$

$$P_{\mathrm{aer}}(r) = K_{\mathrm{aer}} r^{-2} O(r) \beta_{\mathrm{aer}}(r) \exp\left(-2 \int_0^r \alpha(r')\mathrm{d}r'\right) \quad (5.8)$$

in which the terms K_{mol} and K_{aer} contain all range-independent variables. The functions $O(r)$ and the extinction term $\alpha(r)$ given by Eq. (5.4) are the same in the two equations. Once the two constants K_{mol}, K_{aer} or, rather, their ratio $K = K_{\mathrm{mol}}/K_{\mathrm{aer}}$ have been determined, Eqs. (5.7) and (5.8) can be divided, directly yielding the lidar backscatter ratio

$$\Re(r) = \frac{\beta_{\mathrm{aer}}(r)}{\beta_{\mathrm{mol}}(r)} = \frac{K P_{\mathrm{aer}}(r)}{P_{\mathrm{mol}}(r)}. \quad (5.9)$$

High spectral resolution lidars utilize optical filters to distinguish between photons scattered from molecules and those scattered by aerosol or cloud particles. Very narrow bandwidth filters are required (~1 GHz). In addition, the transmitting laser frequency must be locked to the filter center frequency, and the linewidth must be smaller than the filter width (~100 MHz). These requirements make HSRLs more difficult to implement than Raman lidars. However, a HSRL provides much larger molecular signals and can utilize very narrow bandwidths to block solar noise.

5.3 HSRL Implementations

5.3.1 Scanning Fabry–Perot Interferometer

The combined particulate and molecular spectrum can be observed using any frequency-stabilized laser and a scanning Fabry–Perot interferometer. The technique was first proposed and demonstrated by Fiocco et al. [4] using a line-narrowed cw-argon-ion laser and a scanning Fabry–Perot interferometer.

The broadband molecular component of the measured spectrum can be fitted to predictions of a model molecular spectrum. The backscatter ratio can then be determined from the atmospheric density at the measurement altitude and the ratio of the areas under aerosol and molecular scattering curves. Because the filter bandwidth is typically much narrower than the molecular spectrum, the filter rejects most of

the molecular light. This makes the system efficiency low and the measurement time long. Spectral components are measured sequentially, allowing temporal variations of the atmospheric conditions to distort the spectrum. As a result, the spectral scanning approach is unattractive for most atmospheric measurements.

5.3.2 Fixed Fabry–Perot Interferometer

System efficiency can be improved with nonscanning Fabry–Perot systems [5, 6]. In this case the Fabry–Perot etalon is locked to the laser wavelength. Two detectors are employed as shown in Fig. 5.2. One measures the signal passing through the etalon and the other measures the reflected signal. Most of the particulate signal passes through the etalon with only a small fraction reflected. Meanwhile, the Doppler-broadened molecular signal is divided more equally between detectors. If the spectral transmission and reflection characteristics of the etalon are known, a model of the molecular spectrum can be used with an independently supplied atmospheric temperature profile to predict the transmission of the two channels for both particulate and molecular signals. The measured signals in the two channels can then be expressed as linear combinations of the photons scattered from particulate matter and from gas molecules. These equations can be inverted to separate the molecular and particulate component, as is shown in Subsection 5.4.3. For more details see Sroga et al. [7] and Grund et al. [6].

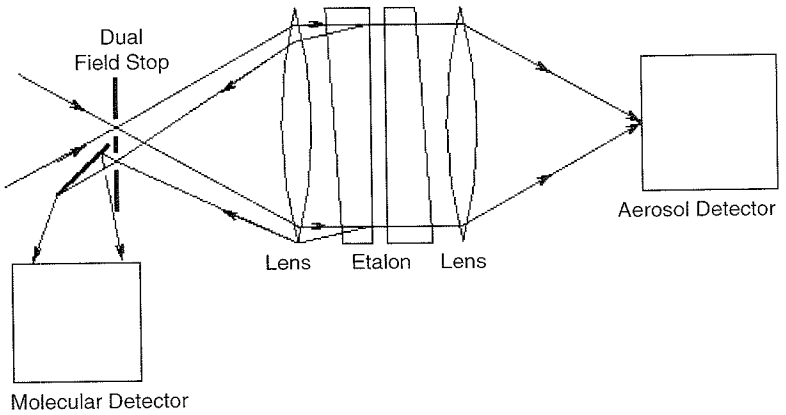

Fig. 5.2. An etalon-based HSRL. The etalon forms a narrow-band filter for light transmitted to the aerosol detector. Light reflected from the etalon is directed to the molecular detector. A pre-filter (not shown) is used to suppress skylight.

The nonscanning etalon approach has several advantages: (1) Errors due to temporal variations in the scattering media are suppressed because both signals are measured simultaneously. (2) System efficiency is improved because the filter bandwidths are larger, and both transmitted and reflected signals are detected. (3) The etalon can be tuned to any wavelength. For example, the system described by Shipley et al. [5] was tuned to operate at the wavelength of an iron Fraunhofer line in the solar spectrum where background solar light is reduced by approximately a factor of five. Or in the case of the system described by Grund et al. [6], the etalon allowed use of a nontunable copper-chloride laser. Also, the lidar may be operated at UV wavelengths, improving eye safety. The major disadvantage of the nonscanning approach lies in the sensitivity of high-resolution etalons to thermal and mechanical perturbations. In addition, at a given spectral resolution the product of the etalon diameter and the angular acceptance of an etalon is limited. Reducing the telescope field-of-view (FOV) can decrease the angular cone of light incident on the etalon. However, practical constraints determine the smallest FOV. The only alternative that will maintain the required spectral resolution as the telescope diameter is increased is to increase the diameter of the etalon plates. As a result, large telescopes require large, expensive etalons. For example, the systems described in Shipley et al. [5] and Grund et al. [6] (350-mm telescopes, 350-μrad FOV), required 150-mm-diameter etalons.

5.3.3 Atomic and Molecular Absorption Filters

Atomic and molecular absorption filters offer an attractive alternative to Fabry–Perot-based systems. Researchers at Colorado State University pioneered this approach using barium vapor filters [8–10]. A dye laser transmitter tuned to a Ba atomic absorption line at a wavelength of 553.7 nm was used in conjunction with heated (700–800 °C) absorption cells containing Ba vapor. Light from the receiving telescope was directed through a beamsplitter with one part of the light sent directly to a detector while the rest of the light was directed through the Ba cell as shown in Fig. 5.3. The central peak of the molecular spectrum and all of the particulate scattering is absorbed, allowing only the spectral wings of the molecular scattering to pass through to a second detector.

The system proposed by Shimizu et al. [8] was designed to simultaneously provide atmospheric temperature measurements and measurements of backscatter coefficients and optical depths. A second

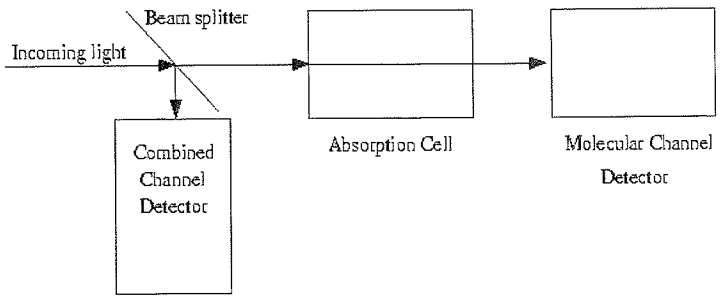

Fig. 5.3. HSRL detector configuration when using an atomic or molecular absorption filter. The absorption filter is evacuated and then filled with the absorbing gas. It is normally enclosed in a temperature-controlled housing to minimize sensitivity to environmental temperature changes. It is important to control the polarization of the incoming light to prevent calibration errors caused by the polarization sensitivity of the beam splitter.

beamsplitter installed behind the first directed part of the light through a second Ba cell. The second cell was maintained at a higher temperature than the first cell in order to increase its spectral width. Because the spectral width of the Doppler-broadened molecular backscatter is proportional to the square root of the temperature, the ratio of the signals seen by the detectors behind the two Ba cells is a function of the atmospheric temperature. The change in signal ratio due to temperature is small, making this a difficult measurement. Additional information on temperature measurements using Ba absorption cells can be found in papers by the Colorado State research group [8–10].

The atomic vapor version of the HSRL replaces the temperature-sensitive and mechanically sensitive Fabry–Perot with a robust and stable atomic absorption filter. It also avoids the acceptance angle limitations of the Fabry–Perot. The major disadvantages of the Ba filter are high operating temperatures and lack of a convenient laser source emitting at the barium absorption wavelength. The Colorado State University group used a Nd:YAG-pumped dye laser as a transmitter in conjunction with the Ba vapor filter.

A much simpler implementation of HSRL is achieved when the Ba cell is replaced with a molecular iodine cell as described by Piironen et al. [11, 12]. (Related information on the use of iodine absorption cells in wind tunnel Doppler velocimetry is found in Forkey [13].) The iodine absorption cell shares the robust spectral stability and wide acceptance angle of the Ba cell while allowing operation at much lower temperatures (~25 to ~100 °C). In addition, it has several suitable absorption

lines within the thermal tuning range of the 532-nm frequency-doubled Nd:YAG laser. (A catalog of iodine absorption lines is provided by Gerstenkorn and Luc [14].) CW-diode-pumped seed lasers are available to injection-lock the laser and generate the necessary narrow spectral line width for the transmitter.

A pair of iodine absorption cells held at different temperatures can also be used to make atmospheric temperature measurements. This work is described in Hair et al. [15] and a PhD thesis by Hair [16].

5.4 HSRL Designed for Remote Operation

The latest University of Wisconsin HSRL employs an iodine absorption cell to separate the molecular signal. It is designed for long-term unattended operation in the Arctic where it will be controlled remotely and operate as an Internet appliance. Use of a high-repetition-rate laser and expansion of the transmitted beam through a 400-mm telescope reduces the transmitted energy density to eye-safe levels. It is possible to look directly into the output beam without hazard. Using the same telescope for the transmitter and receiver makes it easy to maintain stable alignment of the transmitter and receiver although the angular FOV is only 45 μrad. The small FOV and the 4-kHz repetition rate also limit the near-field signal strength, making it possible to record continuous profiles that start at an altitude of ~50 m and extend to 30 km using photon counting detectors. The small FOV also suppresses multiple-scattering contributions. Table 5.1 lists the technical data, Fig. 5.4 presents a sketch of the University of Wisconsin unattended HSRL system.

Table 5.1. UW arctic HSRL technical data

Average transmit power	600 mW	Optical detectors	Geiger-mode APDs, PMT
Pulse repetition rate	4 kHz	APD quantum efficiency	~60%
Wavelength	532 nm	PMT quantum efficiency	~5%
Solar noise bandwidth	8 GHz	Data acquisition	Photon counting
Angular field-of-view	45 μrad	Range resolution	7.5 m
Telescope diameter	400 mm	Maximum time resolution	0.5 s

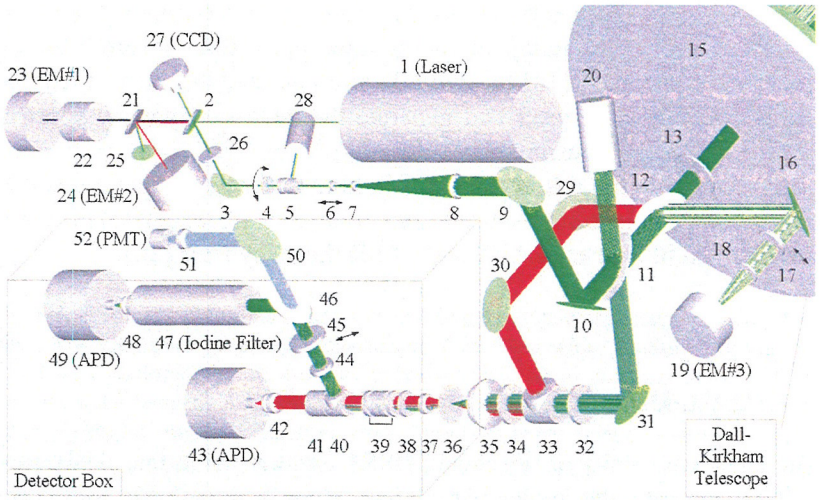

Fig. 5.4. Schematic showing the University of Wisconsin Arctic HSRL system. Component descriptions are provided in Table 5.2. The cross-polarized beam path is shown in red.

Table 5.2. HSRL component descriptions

1 Laser	**27** CCD camera
2 Wedged beamsplitter	**28** Light trap
3 Mirror	**29, 30, 31** Mirrors
4 Half-wave plate	**32, 34** Half-wave plates
5 Glan linear polarizer	**33** Polarizing beamsplitter
6, 7, 8 Beam expander	**35** Gradium + meniscus lens
9, 10 Mirrors	**36** 50-μm field stop
11 Thin-film polarizer	**37** Plano-convex lens
12 8% mirror	**38** Interference filter (.35 nm)
13 Quarter-wave plate	**39** 8-GHz, air-spaced etalon
14 Telescope secondary (not shown)	**40, 41** Polarizing beamsplitter
15 Telescope primary	**42** Gradium+meniscus lens
16 Black glass flat	**43** APD detector (dia = 170 μm)
17 Removable ND filter, OD = 3	**44** Half-wave plate
18 Plano-convex lens	**45** Insertable OD = 3 filter
19 Transmitted-energy monitor	**46** Beamsplitter
20 Light trap	**47** 272-mm long I_2 cell
21 Wedge	**48** Gradium + meniscus lens
22 Calibration iodine cell	**49** APD detector
23, 24 I_2-locking energy monitors	**50** Mirror
25 Mirror	**51** Plano-convex lens
26 Mirror, R = 1/2%	**52** PMT detector

5.4.1 Transmitter

The laser transmitter (1) is a diode-pumped, intracavity, frequency-doubled Nd-YAG laser. Narrow-band, single-frequency operation is provided by injection seeding with a single-frequency, cw-diode-pumped diode laser. The main laser cavity is maintained in resonance with the seed laser by adjusting the cavity length to minimize the time between the Q-switch trigger and the emission of the laser pulse. The emission wavelength is tuned via temperature control of the seed laser crystal and is locked to line #1109 of the iodine absorption spectra (line numbers from [14]). Locking is accomplished by minimizing the transmission through a 2-cm-long iodine absorption cell (22). Energy monitors (23) and (24) are used to measure the transmission. A half-wave plate (4) mounted in a computer-controlled rotation stage and a Glan–Thompson polarizer (5) allow computer control of the emitted power without changing the operating characteristics of the laser; this power control is used during system calibration.

A small beam expansion telescope (6–8) enlarges the ~1-mm laser beam to overfill a 20-mm aperture. Overfilling wastes some of the laser power but serves to flatten the energy distribution in the beam. This allows more energy to be transmitted without exceeding eye-safety limits at any point within the output aperture. The linearly polarized transmit beam is converted to circular polarization by a quarter-wave plate (13) and then expanded by a 20× afocal telescope (15) to a final diameter of 400 mm.

CCD camera (27) images interference fringes formed by reflections from the mirror (25) and a partially reflective mirror (26). The motion of these fringes is used to determine the laser frequency while tuning the laser during calibration. An absolute calibration of the fringe information is derived from known positions of the iodine absorption lines.

5.4.2 Receiver

The receiver and transmitter use the same afocal telescope (14,15). This greatly simplifies the task of maintaining alignment between the transmitted beam and the receiver field of view and permits the lidar to operate with a 45-μrad FOV. The telescope directs the received photons through the quarter-wave plate (13). Received photons that have maintained their polarization (except for the reversal which occurs on changing their direction of propagation) are converted into linear polarization with its axis of polarization perpendicular to that of the transmitted photons. A portion of these photons and part of the photons whose polarization has

been changed by the scattering media are separated by a beamsplitter comprised of a glass plate (12) that is antireflection coated on one surface and uncoated on the other. This beamsplitter directs 12% of the cross-polarized photons to the input of a polarizing cube (33) where the beam is combined with the rest of the signal for transmission through the field stop and the background noise filter. This signal is used to measure depolarization of the return signal. Meanwhile, the photons that did not have their polarization changed by scattering and have managed to pass through the cross-polarization pick-off (12) encounter the thin-film polarizer that forms the transmit/receive switch (11) and are directed to the other entrance face of the polarizing cube (33). This element combines parallel and cross components of polarization into a single beam and maintains their orthogonal linear polarizations. The combined beam is then focused by lens (35) onto the 50-μm-diameter pinhole (36) that defines the receiver FOV. After collimation by lens (37), both beams pass through a skylight background filter comprised of a 0.35-nm-bandpass interference filter (38) followed by an 8-GHz-bandpass pressure-tuned etalon. Air pressure within the etalon chamber is computer-controlled via a stepper-motor-driven stainless-steel bellows. At this point polarization cube (40) separates the parallel-polarization signal from the cross-polarized component and passes the cross component on to a second polarizer (41) that removes any residual parallel polarization. The cross-polarized signal is then detected by a Geiger-mode avalanche photodiode (APD) photon-counting module (43). The APD is used in this channel because it offers higher quantum efficiency (~60%) than is available in a PMT. A neutral density filter (OD = 3) (44) is inserted into the optical path during calibration. This filter, plus a power reduction achieved via a rotation of the half-wave plate (4), reduces the number of photons scattered from optical surfaces in the lidar so that they can be counted without large pile-up corrections. This allows the scattered light pulse to be used in the calibration of the spectral bandpass of the lidar. The polarization sensitivity of the beamsplitter (46) along with the rotation of the half-wave plate (44) is used to balance signal strengths at the combined (52) and at the molecular (49) detectors. The beamsplitter sends part of the signal to a photon-counting PMT detector (52), which detects a signal containing both particulate and molecular scattered photons. A PMT is used here because it can accommodate high photon counting rates that are generated by dense, low-altitude clouds. The other component of the parallel-polarized light leaving the beamsplitter (46) is directed through a 272-mm iodine absorption cell (47) and focused

onto a second Geiger-mode APD photon-counting module (49). A high-QE APD detector can be used in this channel because the iodine filter blocks the intense particulate scattering signal from clouds. The entire system except for the telescope is housed in a temperature-controlled enclosure to minimize both thermally induced alignment changes and changes in the spectral characteristics of the iodine absorption cells. In addition, the iodine cells are operated at 30°C: this is ~2 K above the temperature at which all of the iodine in the cell evaporates. The temperature sensitivity of the cell is reduced because the iodine vapor density does not change in response to condensation and evaporation of iodine.

5.4.3 Calibration

The signals S_c and S_m detected in the combined channel and in the molecular channel, respectively, can be described as a linear combination of the number N_a of aerosol photons and the number N_m of molecular photons incident on the lidar receiver:

$$S_c = N_a + C_{mc} N_m, \tag{5.10}$$

$$S_m = C_{am} N_a + C_{mm} N_m. \tag{5.11}$$

The equations have been normalized relative to the response of the combined channel to aerosol photons. This normalization is possible because an absolute calibration is generated by comparing the observed molecular lidar return to the lidar return computed from Rayleigh scattering theory. C_{mc} describes the relative contribution of molecular photons to the combined channel. C_{mc} may be less than unity if the pre-filter used to block sunlight is sufficiently narrow to affect the transmission of the Doppler-broadened molecular scattering. C_{am} describes the response of the molecular channel to aerosol photons and accounts for the on-line leakage of the absorption filter. C_{mm} describes the transmission of molecular photons through the absorption filter. Equations (5.10) and (5.11) can be inverted to compute the relative number of aerosol and molecular photons incident on the system:

$$N_a = \frac{C_{mm} S_c - C_{mc} S_m}{C_m - C_{am} C_{mc}}, \tag{5.12}$$

$$N_m = \frac{S_m - C_{am} S_c}{C_{mm} - C_{am} C_{mc}}. \tag{5.13}$$

The coefficients C_{am}, C_{mm}, and C_{mc} are determined by directing a sample of the transmitted beam into the receiver while scanning the laser frequency. The spectral transmissions (see Fig. 5.5) for the molecular and combined channel are then convolved with the Doppler-broadened molecular spectrum, which is computed from theory and independently supplied temperature data. C_{mm} and C_{mc} are the values of the molecular and combined convolution functions at the operating frequency of the laser. Because C_{mm} and C_{mc} are temperature and pressure dependent, they must be computed as functions of altitude. C_{am} is taken directly from the measured leakage of the absorption filter at the operating frequency of the laser.

In the lower atmosphere, Brillouin scattering causes the Doppler-broadened molecular line shape to vary slightly from the Gaussian profile predicted for a Maxwellian velocity distribution. A line-shape model that

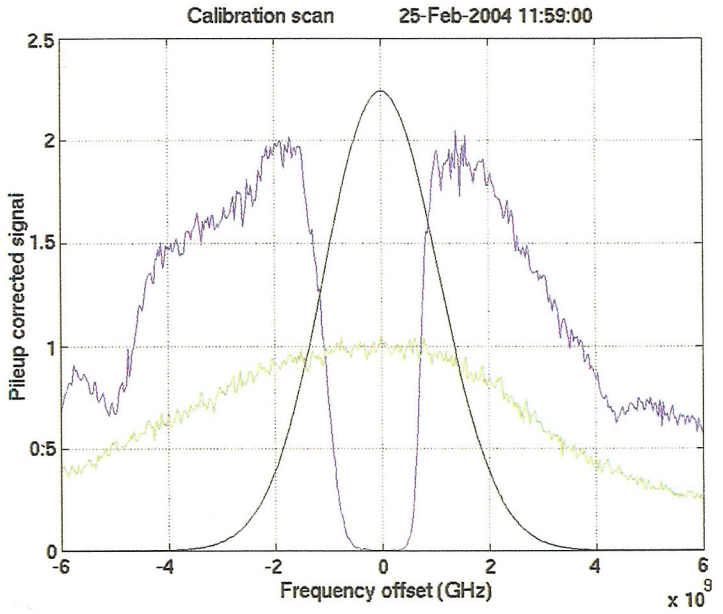

Fig. 5.5. Calibration scan showing the transmission of the molecular (blue) and combined (green) channels as a function of frequency. The Doppler broadened molecular spectrum for 300 K is also shown (black). Line 1109 of the iodine absorption spectrum (central notch) rejects most of the aerosol scattering and the central portion of the molecular scattering while passing the wings of the molecular line. The spectral transmission of the combined channel is determined by the pre-filter etalon.

includes Brillouin scattering is described by Tenti et al. [17] and a Fortran computer implementation can be found in Forkey [13].

5.5 Data Examples

Figures 5.6–5.11 present data acquired with the University of Wisconsin HSRL. Figure 5.6 shows an attenuated backscatter-coefficient image acquired on 14 January 2004. The data represent the output of the combined channel corrected for the squared distance, for laser pulse energy, and for the laser-beam FOV overlap function. They are not corrected for attenuation but normalized using the molecular signal to show the correct backscatter coefficient at an altitude of 75 m. A well-calibrated conventional lidar would produce an identical image. Note how the cirrus cloud at 7 km is shadowed by the 3.4-km water cloud that appears at 6:10 UTC. Also note the strong lidar return seen below the clouds as a result of the combined effect of aerosol and molecular scattering. Data gaps at 8 and 12 UTC occur during system calibrations.

Using the same data set, Fig. 5.7 presents the backscatter coefficient derived from both the molecular and combined-channel data. This image is calibrated absolutely, molecular scattering has been removed. Areas with insufficient signal for the HSRL inversion are indicated by black shadows; everywhere else, attenuation has been removed. Note the effect of attenuation correction on the appearance of the 7 km cirrus cloud. The lower cloud no longer affects the scattering coefficient measured above.

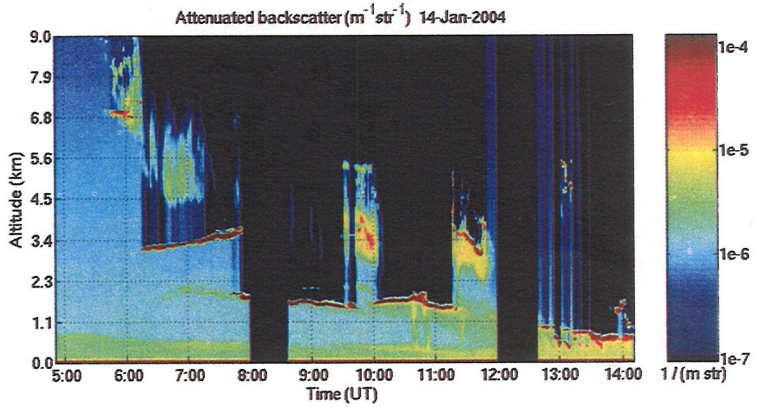

Fig. 5.6. Attenuated backscatter image recorded with the HSRL on 14 January 2004.

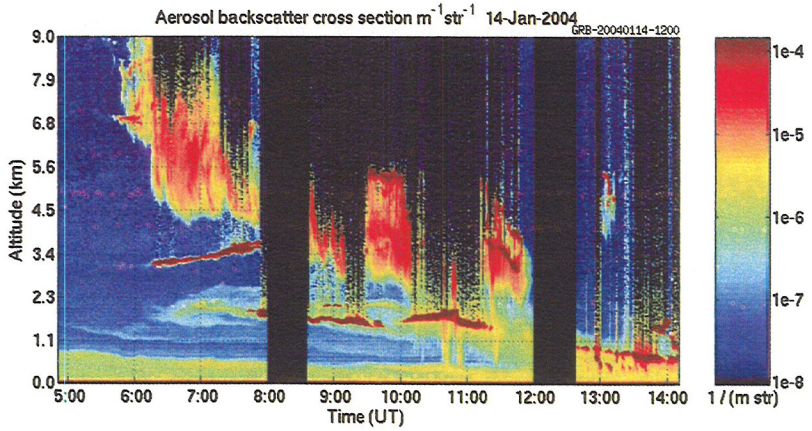

Fig. 5.7. Aerosol backscatter coefficient recorded on 14 January 2004.

As long as sufficient signal is available the measurements are unchanged. Also note how removal of the molecular scattering increases contrast in the aerosol structure below the clouds (i.e., at 2 km and 7 UTC).

The UW Arctic HSRL transmits circularly polarized light. The receiver separates the returned signal into two left and right-handed components. Light scattered from spherical particles is not depolarized and is returned to the combined and molecular channels. A portion of

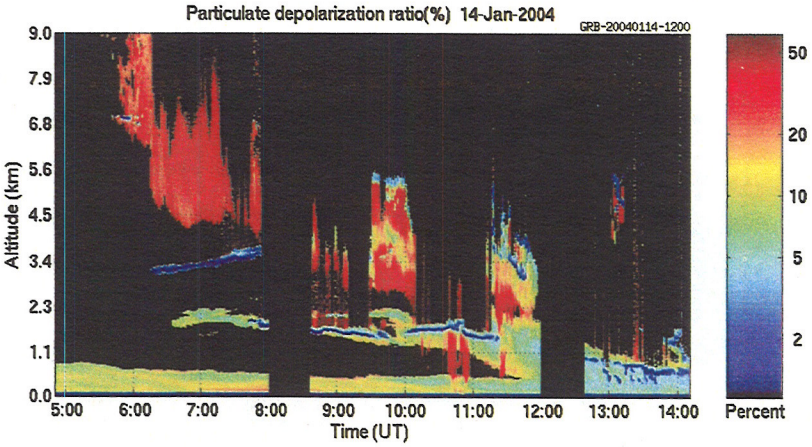

Fig. 5.8. Circular depolarization ratio recorded on 14 January 2004. Note the logarithmic scale.

the light scattered by nonspherical particles is depolarized. The cross-polarized channel measures this signal. Figure 5.8 shows the circular depolarization ratio computed from these signals. As expected, light backscattered from water clouds maintains the transmitted polarization and exhibits very low depolarization (<1%) while ice clouds show high depolarization (~40%). Aerosol depolarization often varies between 0 and 15% depending on the type of aerosol; water hazes exhibit very low depolarization while irregularly-shaped dust particles show larger values.

Figure 5.9 shows the aerosol backscatter ratio measured in the relatively clear period before 5:30 UTC. These values were computed from the calibration scan and a radiosonde temperature profile. Near 9 km the scattering-ratio profile shows a minimum value of (−0.024). This layer is likely to be nearly aerosol-free due to scavenging by the cirrus cloud above. The negative value gives an indication of the error present. It is due to a combination of lidar characterization errors and errors in the temperature profile. The temperature profile was obtained from a

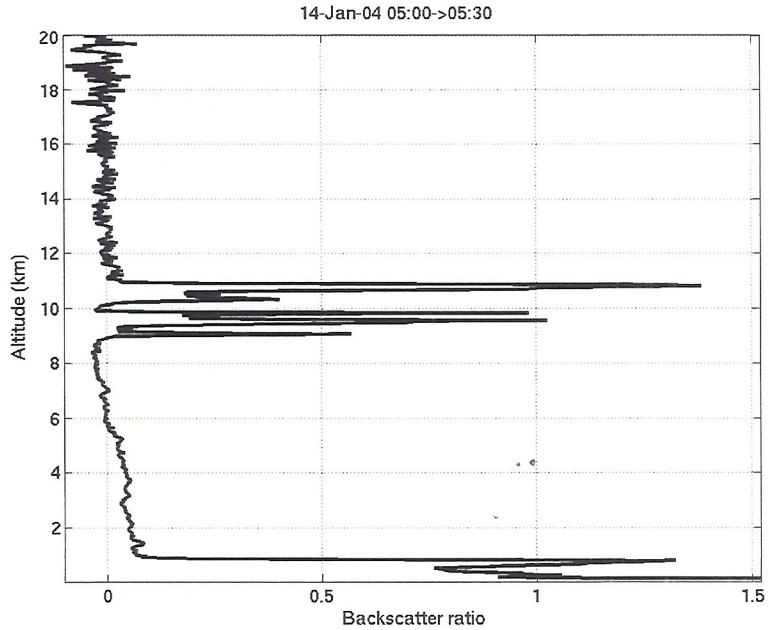

Fig. 5.9. Scattering ratio profile measured between 5:00 and 5:30 UTC on 14 January 2004.

radiosonde launched about 5 hours earlier at a weather station approximately 150 km from the lidar. The HSRL technique makes it possible to compute rigorous error estimates [12]. However, this is a new lidar and system characterization is still in progress so this has not been completed.

Figure 5.10 shows backscatter coefficient profiles measured between 6:40 and 6:41 UTC. The basis of the HSRL optical depth measurement is easily seen in comparing the attenuated molecular profile to the Rayleigh backscatter profile computed from radiosonde data. The wide dynamic range of the lidar is also evident. This figure shows measurements ranging over five decades. When the time averaging is increased to a few minutes, the instrument can provide measurements over a range of more than six decades. Careful data processing is required to maintain accuracy over this wide dynamic range. Background sky noise and dark counts must be subtracted. Pileup correction must be applied to properly represent signals at high count rates. Detector afterpulse corrections

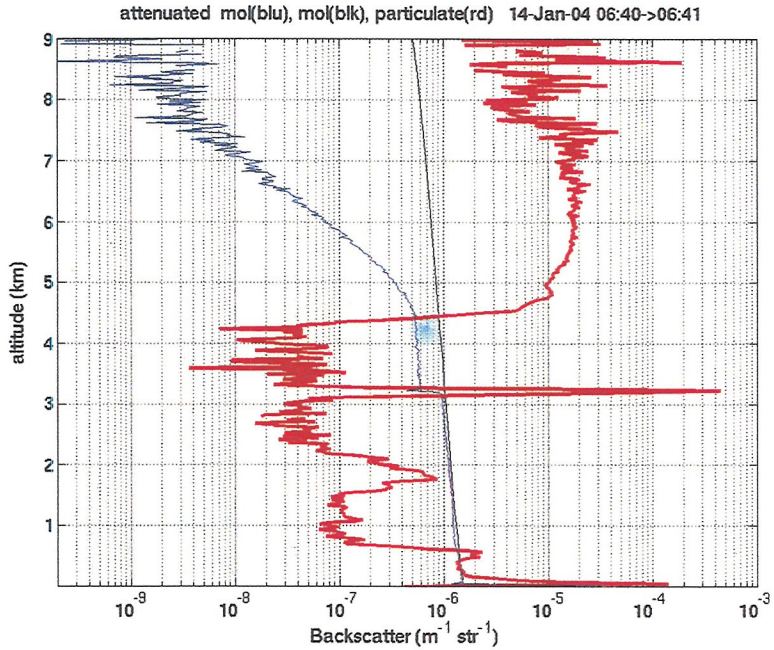

Fig. 5.10. The one-minute average aerosol backscatter-coefficient profile (red) and the attenuated molecular return (blue) observed between 6:40 and 6:41 UTC. The Rayleigh return computed from the 00 UTC Green Bay, Wisconsin, radiosonde is shown in black.

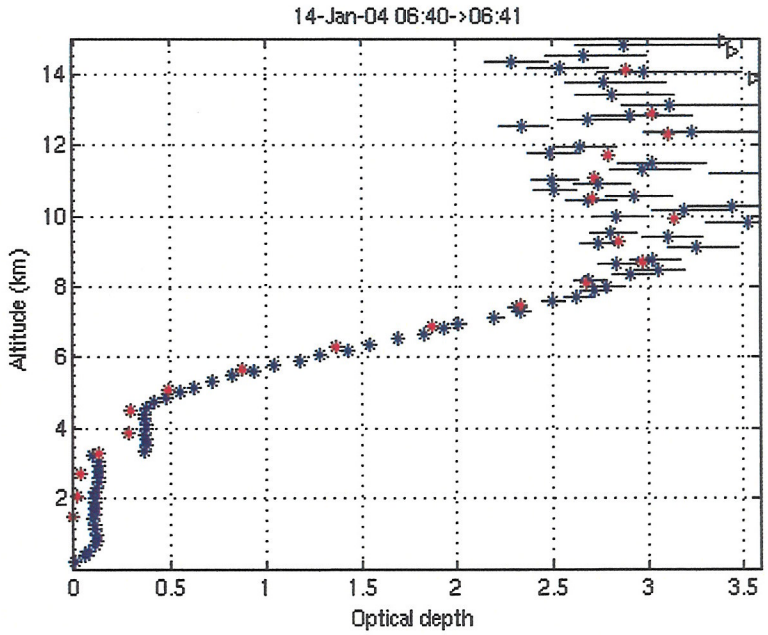

Fig. 5.11. Optical depth profiles derived for a one-minute time average and altitude averages of 150 m (blue) and 600 m (red).

must be carried out to remove spurious counts generated by previously detected photons [12].

Figure 5.11 shows the optical depth as a function of altitude derived for a 1-minute average between 6:40 and 6:41 UTC. These data were computed using 150 m (blue) and 600 m (red) vertical averages. Uncertainty estimates based on photon counting errors are shown. In this case, photon statistics dominates the noise. Longer time averages reduce the statistical error. However, other factors, such as detector after-pulsing, limit the maximum optical depth that can be measured to ~4.

5.6 Future Prospects

HSRL, if built along the lines followed in the design of the University of Wisconsin Arctic High-Spectral-Resolution Lidar, offers a unique combination of advantages: (1) robust calibration and no unstable inversions or a-priori assumptions required to derive scattering coefficients and optical depths; (2) eye-safe operation that allows direct viewing of

the transmitted beam while operating at the wavelengths most important for human vision and most important for the transfer of solar radiation in the atmosphere; (3) photon counting detectors allowing simple robust calibration; (4) large dynamic range allowing the system to operate without regard to atmospheric conditions—no operator is required to change parameters in response to varying atmospheric conditions; (5) narrow angular field-of-view that limits multiple scattering in water clouds to negligible levels and reduces background sky noise; (6) automatic data processing possible because the signals contain sufficient information to derive products without ambiguity; (7) profiles normalized to atmospheric molecular scattering and independent of window transmission—the lidar continues to make accurate measurements even though the external window transmission is degraded by water, snow, or dirt.

Despite these advantages, few HSRL systems have been constructed; technical complexity has limited deployment. A single-mode laser with a spectral linewidth below 100 MHz is required. Separation of the aerosol and molecular return requires a filter with a bandwidth of approximate 1 GHz. The laser and the filter must be frequency-locked to within approximately 100 MHz. High repetition rate systems also require an etalon pre-filter to limit skylight and very narrow field-of-view receivers with stringent requirements to maintain filter tuning and transmitter/receiver alignments.

Advances in technology have greatly reduced the challenges associated with the HSRL technique. High repetition rate, injection-seeded, diode-pumped Nd:YAG lasers are available as standard commercial products. These lasers consume a few hundred watts of power and operate for thousands of hours without maintenance. They replace flashlamp-pumped lasers that used kilowatts of power and required maintenance at ~100-hour intervals. Simple, robust and stable, iodine absorption filters replace the environmentally sensitive Fabry–Perot etalon used to separate the molecular and aerosol returns. Photomultiplier tubes are replaced by Geiger-mode avalanche-photodiodes as high-quantum-efficiency photon-counting detectors in simple-to-use packages.

In the near future, fiber amplifiers will boost the power of miniature narrow-band lasers to the levels required by HSRL systems. These will further reduce the power consumption, volume, and cost of the transmitter. They will operate for tens of thousands of hours without maintenance and will eliminate the requirement for water cooling. It also appears

likely that iodine absorption filters will be constructed with hollow-core photonic-crystal fibers and that fiber components will replace many of the traditional optical elements in the receiver.

Until now, HSRLs have been in use at a limited number of research laboratories. The intrinsic advantages of the HSRL technique, coupled with advancing technology, are likely to greatly expand its deployment and to make high spectral resolution lidar a routine observational instrument in service at numerous automated weather stations and airports around the world.

References

[1] A.T. Young: Physics Today **35**(1), 42 (1982)
[2] B.A. Bodhanine, E. G. Dutton, J. R. Slusser: J. Atmos. Ocean. Techn. **16**, 1851 (1999)
[3] R.M. Measures: *Laser Remote Sensing* (Wiley-Interscience, New York 1984), p. 42
[4] G.G. Fiocco, G. Beneditti-Michelangeli, K. Maischberger, et al.: Nature **229**, 78 (1971)
[5] S.T. Shipley, D.H. Tracy, E.W. Eloranta, et al.: Appl. Opt. **22**, 3716 (1983)
[6] C.J. Grund, E.W. Eloranta: Opt. Eng. **30**, 6 (1991)
[7] J.T. Sroga, E.W. Eloranta, S.T. Shipley, et al.: Appl. Opt. **22**, 3725 (1983)
[8] H. Shimizu, S.A. Lee, C.Y. She: Appl. Opt. **22**, 1373 (1983)
[9] H. Shimizu, K. Noguchi, C. She: Appl. Opt. **25**, 1460 (1986)
[10] C.Y. She, Alvarez II, L.M. Caldwell, et al.: Optics Letters **17**, 541 (1992)
[11] P. Piironen, E.W. Eloranta: Optics Letters **19**, 234 (1994)
[12] P. Piironen: A high spectral resolution lidar based on an iodine absorption filter. University of Joensuu PhD thesis, Joensuu, Finland (1994)
[13] J.N. Forkey: Development and demonstration of filtered Rayleigh scattering—a laser based flow diagnostic for planar measurement of velocity, temperature and pressure. Princeton University PhD thesis, Princeton, NJ (1996)
[14] S. Gerstenkorn, P. Luc: *Atlas du spectre d'absorption de la molécule d'iode* (Centre National de la Recherche Scientifique, Paris 1978)
[15] J.W. Hair, L.W. Loren, M. Caldwell, et al.: Appl. Opt. **40**, 5280 (2001)
[16] J.W. Hair: A high spectral resolution lidar at 532 for simultaneous measurement of atmospheric state and aerosol profiles using iodine vapor filters. Colorado State University PhD thesis, Fort Collins, CO (1998)
[17] G. Tenti, C.D. Boley, R.C. Desai: Canadian Journal of Physics **53**, 285 (1974)